Monthly Notices of the ROYAL ASTRONOMICAL SOCIETY

MNRAS **531,** 2415–2421 (2024) https://doi.org/10.1093/mnras/stae1294
Advance Access publication 2024 May 20

Candidates for downstream jets at interplanetary shocks

H. Hietala [1,2,3★] D. Trotta [2] A. Fedeli,[3] L. B. Wilson, III,[4] L. Vuorinen[3] and J. T. Coburn[5,6]

[1]*Department of Physics and Astronomy, Queen Mary University of London, Mile End Road, London E1 4NS, UK*
[2]*The Blackett Laboratory, Department of Physics, Imperial College London, Prince Consort Road, London SW7 2AZ, UK*
[3]*Department of Physics and Astronomy, University of Turku, Vesilinnantie 5, Fl-20500 Turku, Finland*
[4]*NASA Goddard Space Flight Center, Greenbelt, MD 20771, USA*
[5]*Mullard Space Science Laboratory, University College London, Holmbury St. Mary, Dorking RH5 6NT, UK*
[6]*Space Science Institute, 4765 Walnut St, Suite B, Boulder, CO 80301, USA*

Accepted 2024 May 14. Received 2024 May 13; in original form 2023 December 10

ABSTRACT

Localized dynamic pressure enhancements arising from kinetic processes are frequently observed downstream of the Earth's bow shock. These structures, called jets, modify their plasma surroundings and participate in particle energization. Here, we report the first observations of jet-like structures in a non-planetary shock environment: downstream of interplanetary shocks. We introduce an analysis approach suitable for such conditions and apply it to Wind spacecraft data. We present one event with a Mach number similar to the Earth's bow shock as a benchmark, as well as two low Mach number, low beta shocks: a parameter range that is difficult to access at planets. The jet-like structures we find are tens of ion inertial lengths in size, and some are observed further away from the shock than in a limited magnetosheath. We find that their properties are similar to those of magnetosheath jets: in the frame of the shock these structures are fast, cold, and most have no strong magnetic field variations. All three interplanetary shocks feature foreshock activity, but no strongly compressive waves. We discuss the implications, these findings have for the proposed jet formation mechanisms.

Key words: plasmas – shock waves – solar wind.

1 INTRODUCTION

Localized dynamic pressure enhancements – jets – are regularly observed downstream of the Earth's bow shock (Plaschke et al. 2018). They drive enhanced particle acceleration (Liu et al. 2019, 2020a, b), large amplitude magnetic field variations (Vuorinen et al. 2021), and reconnecting current sheets (Eriksson et al. 2016). Various simulations, of both global bow shocks (e.g. Karimabadi et al. 2014; Palmroth et al. 2018; Guo et al. 2022) and local planar shocks (e.g. Hao et al. 2016; Preisser et al. 2020; Tinoco-Arenas et al. 2022), have also exhibited downstream jets, suggesting that they are not unique to the Earth's magnetosheath. Similar pressure pulses have recently been reported at Mars (Gunell et al. 2023).

A series of recent studies have investigated shock conditions favourable for jet formation using large statistics gathered in the subsolar magnetosheath (Vuorinen, Hietala & Plaschke 2019; Raptis et al. 2020; LaMoury et al. 2021; Koller et al. 2023; Vuorinen et al. 2023). Summarizing some of the key findings, they have found, first, that jets are ∼9 times more common downstream of the quasi-parallel shock (where the angle θ_{Bn} between the shock normal and upstream magnetic field is small) than the quasi-perpendicular (where θ_{Bn} is large) (Vuorinen et al. 2019). Secondly, jet occurrence rates during quasi-parallel geometry appear to be constant for all upstream conditions for Alfvén Mach number $M_A \gtrsim 5$ and plasma $\beta \gtrsim 0.5$. And thirdly, jets under quasi-perpendicular geometry are favored by increasing M_A and β (Vuorinen et al. 2023). This is driven by lower upstream magnetic field magnitude, which increases the spatial scale sizes of shock rippling and self-reformation.

Multiple mechanisms may produce jet-like structures. Proposed mechanisms include upstream magnetic directional discontinuities interacting with the shock (e.g. Archer, Horbury & Eastwood 2012), shock surface ripples or corrugations (e.g. Hietala et al. 2009, 2012), transmission of foreshock compressive magnetic structures (e.g. Karlsson et al. 2018; Palmroth et al. 2018; Suni et al. 2021), and shock reformation (Raptis et al. 2022). Under which conditions each mechanism dominates remains an open question.

It is therefore important to investigate other shock conditions that are different from or rare for the Earth's bow shock. Interplanetary (IP) shocks offer an opportunity to extend downstream jet analysis to new parameter regimes: IP shocks have a much larger radius of curvature than planetary bow shocks. IP shocks at 1 au generally have lower Mach numbers than the Earth's subsolar bow shock during low shock obliquity, and can have lower plasma beta (Kilpua et al. 2015; Vuorinen et al. 2023). Additionally, IP shocks typically have less compressive/steep upstream waves (Kajdič et al. 2012; Blanco-Cano et al. 2016).

In this study, we search for similar jet-like dynamic pressure pulses downstream of interplanetary shocks observed by the Wind spacecraft (Wilson et al. 2021). We start by describing how the jet selection criteria are adapted for such conditions. We first show an example of a strong, quasi-parallel interplanetary shock comparable

★ E-mail: h.hietala@qmul.ac.uk

to the Earth's bow shock to demonstrate our methods. We then present two low Mach number, low plasma beta events to explore a new parameter range. The interplanetary shocks where we have found jet candidates feature foreshock activity, a favourable condition for jet formation according to bow shock studies. We examine the properties of the candidate jets and compare them to those reported for magnetosheath jets, finding them to be very similar. We finish by discussing how this widening of the range of environments where downstream jets are observed can shed light on their dynamics and formation mechanisms.

2 METHODS

2.1 Selection criteria

Jets are thought to arise from ion kinetic phenomena, distinctive with respect to a magnetohydrodynamic (MHD) background. Let us consider the selection criteria to identify them. The Rankine–Hugoniot conditions relate upstream (subscript 1) to downstream (subscript 2) conditions in the frame of the shock. From the conservation of mass across the shock front ($[\rho V_\mathrm{n}] = 0$), we get

$$\frac{\rho_2}{\rho_1} = r, \tag{1}$$

and

$$\frac{V_{2\mathrm{n}}}{V_{1\mathrm{n}}} = \frac{1}{r}. \tag{2}$$

Here, ρ is the density, V_n the component of velocity normal to the shock, and r is the (gas) compression ratio. In other words, the density is increased, and the bulk flow speed normal to the shock is decelerated, on average. Hence, the downstream dynamic pressure in the shock normal direction is

$$P_{\mathrm{dyn2,n}} = \rho_2 V_{2\mathrm{n}}^2 = r\rho_1 \left(\frac{1}{r}V_{1\mathrm{n}}\right)^2 = \frac{1}{r}\rho_1 V_{1\mathrm{n}}^2 = \frac{1}{r}P_{\mathrm{dyn1,n}}. \tag{3}$$

That is, downstream dynamic pressure in the direction normal to the shock is reduced according to the compression ratio.

Searching for downstream jets, we will be looking for brief instances where the downstream dynamic pressure in the shock frame is enhanced above this MHD (background) level. Here, we set the threshold at twice the expected background dynamic pressure ratio:

$$\left.\frac{\rho_2 V_{2\mathrm{n}}^2}{\langle \rho_1 V_{1\mathrm{n}}^2 \rangle}\right|_{\text{shock frame}} > 2 \times \frac{1}{r}, \tag{4}$$

where the upstream average needs to be taken over a scale appropriate to the shock under study. Furthermore, we require that these pressure enhancements should feature a localized, brief enhancement in the downstream $V_{2\mathrm{n}}$ (in comparison to equation (2)), i.e. corresponding to fast, less decelerated plasma parcels.

For comparison, let us consider the special case of the subsolar region of the Earth's bow shock which generally has a high Mach number with $r \sim 4$ and the X_{GSE} direction is a proxy for the shock normal, and where the shock frame can be approximated with the spacecraft frame (sc). Then, the above criteria reduce to

$$\left.\frac{\rho_{\mathrm{msh}} V_{\mathrm{X,GSE}}^2}{\langle \rho_{\mathrm{SW}} V_{\mathrm{SW}}^2 \rangle}\right|_{\text{sc frame}} > 0.5, \tag{5}$$

and a brief, pulse-like enhancement in $-V_{\mathrm{X,GSE}}$ with respect to their surroundings. These are the main criteria used by, e.g. Plaschke, Hietala & Angelopoulos (2013) and many other magnetosheath studies.

The relations (2) and (4) are appropriate for shock waves in general, including simulations and interplanetary shocks, and will therefore be used here. Note, however, that they are sensitive to the estimation of the shock normal vector $\boldsymbol{n}$ and shock speed $V_{\mathrm{sh}}^{\mathrm{sc}}$ in the spacecraft frame, which introduces uncertainty. We will address this uncertainty with our data analysis approach described in Section 3.

2.2 Expected jet duration

In order to identify potential jet signatures from spacecraft observations in the fast flowing solar wind, we need to consider their expected spatial size and the corresponding temporal duration in a time-series. Statistics from the magnetosheath show that the typical jet durations are few tens of seconds under quasi-parallel geometry, and significantly shorter under quasi-perpendicular conditions (Plaschke et al. 2020; Raptis et al. 2020; Vuorinen et al. 2023). Focusing on the larger, quasi-parallel jets, an estimated jet size parallel to the flow $D_{||} \sim 0.5\,R_\mathrm{E}$ would correspond to ∼30–35 d_i in the magnetosheath, where R_E is the Earth radius and d_i the ion inertial length. This would be ∼2600 km in the solar wind at 1 au. In the spacecraft frame, the duration of the jet would then be 4–7 s in 400 km s^{-1} solar wind, and 3 s in 700 km s^{-1} solar wind, which would be the more common case downstream of an interplanetary shock. This places a requirement on the cadence of the plasma instrument suitable for this interplanetary shock jet investigation.

3 DATA AND ANALYSIS APPROACH

The Wind spacecraft (Wilson et al. 2021) has a high plasma cadence (∼3 s), a large data base of IP shocks to search for relevant upstream conditions (e.g., by M. L. Stevens and J. C. Kasper at https://www.cfa.harvard.edu/shocks/wi_data/), and it is not much affected by the Earth's foreshock.

In this study, we use Wind data from the flux gate magnetometer (MFI; Lin et al. (1995)) and the electrostatic analyser 3DP/PESA-Low (Lepping et al. 1995). We compared the 3DP plasma moments with the lower cadence Faraday cup measurements (SWE; Ogilvie et al. (1995)), to ensure that there is a good overall agreement. We include 3DP on-board calculations of ion temperature anisotropy, which were recently used also in (Coburn, Chen & Squire 2022).

We calculated 20 different estimates for the shock normal vector $\boldsymbol{n}$ and the shock speed in the spacecraft frame $V_{\mathrm{sh}}^{\mathrm{sc}}$ using the SerPyShock (Trotta et al. 2022) to overcome some of the issues related to the sensitivity of jet selection criteria (4) to the shock parameters. Window sizes upstream and downstream were varied systematically between 1 and 6 min, and in relatively stable regions as appropriate to each event. The shock normal estimation is done using the Mixed Mode 3 method (MX3; see Schwartz (2000)) and then the shock speed using the Mass Flux Algorithm (Schwartz 2000) with the corresponding windows. We required that the downstream normal velocity $V_{2\mathrm{n}}^{\mathrm{sh}}$ in the shock frame stays mainly negative (away from the shock) for minutes after the shock. This led to discarding some window combinations. Twenty ($\boldsymbol{n}$, $V_{\mathrm{sh}}^{\mathrm{sc}}$) pairs were randomly extracted from the resulting distribution. We use the spread resulting from these twenty estimates to quantify the uncertainty of shock parameters.

To characterize the environment near a shock, we use 5 min windows on each side of the shock (excluding ±30 s around the shock ramp) to calculate the average upstream and downstream properties. Five minutes is sufficiently longer than the upstream fluctuations and the expected downstream jet duration. For quantities that depend on the shock normal and speed, we do the calculation

Table 1. Characteristics of each shock event. The angle brackets ⟨⟩ indicate average over the 20 normal and speed estimates.

#	Date	GSE location [R_E]	$\langle\theta_{Bn}\rangle$ [°]	$\langle V_{sh}^{sc}\rangle$ [km s^{-1}]	r	$\langle M_{fm}\rangle$	$\langle M_{An}\rangle$	β_1	$T_{1\|\|}/T_{1\perp}$
1	2021-11-03	(197, 14.7, −10.5)	12	801	4.4	6.0	7.0	0.4	1.5
2	1999-12-12	(−12.6, −56.5, 16.2)	49	580	2.5	1.8	3.0	0.07	1.7
3	2000-02-11	(127, −5.5, 8.7)	36	502	2.4	1.6	2.1	0.3	1.3

for all the twenty estimates and take the mean (noted by the angle brackets ⟨⟩ without a subscript). These include the fast mode Mach number $M_{fm} = \frac{V_{ln}^{sh}}{V_{fm}(V_S, V_A, \theta_{Bn})}$ and the Alfvén Mach number in the de Hoffmann–Teller frame $M_{An} = \frac{V_{ln}^{sh}\sqrt{\mu_0 \rho_1}}{B_{ln}}$. Here, V_S is the sound speed and V_A is the Alfvén speed. The parameter ranges in the text refer to the minimum/maximum values obtained across the twenty $(\boldsymbol{n}, V_{sh}^{sc})$ estimate pairs.

We use two diagnostic quantities in order to relate the Wind observations to the general jet selection criteria described in Section 2.1: the ratio of normal component of the velocity and its upstream average, in the shock frame

$$-V_n^{sh}\,\text{ratio} = \frac{-V_n^{sh}(t))}{\left\langle V_{ln}^{sh}\right\rangle_{5\,\text{min}}}, \tag{6}$$

and the dynamic pressure ratio in the shock frame

$$P_{dyn,n}^{sh}\,\text{ratio} = \frac{P_{dyn,n}^{sh}(t))}{\left\langle P_{dyn1,n}^{sh}\right\rangle_{5\,\text{min}}}. \tag{7}$$

The first has a negative sign as the shock normal vector points towards the upstream. We calculate these ratios using each of the 20 shock normal and speed estimate pairs, producing 20 curves in the time series. The temporal averages are calculated in the 5 min upstream windows for each estimate. We use these normalized (ratio) quantities as they ensure that the threshold values stay fixed for all the 20 curves, while the spread of the curves in the downstream will indicate estimation uncertainty. The $-V_n^{sh}$ ratio should be, by construction, on average equal to −1 with some temporal variation in the upstream region, and is expected to be around $-1/r$ in the downstream region (MHD; equation 2). The dynamic pressure ratio is similarly equal to 1 in the upstream and is expected to be around $1/r$ in the downstream region (MHD; equation 3). A downstream jet would then be a localized enhancement of the dynamic pressure ratio above the threshold of $2/r$ (equation 4), and feature a (negative) localized enhancement in the $-V_n^{sh}$ ratio. In the figures, we highlight with blue vertical shading those jet candidates where the dynamic pressure threshold is exceeded for more than half of the 20 estimates. We then visually inspect the candidates for V_n^{sh} ratio variations.

4 RESULTS

The main characteristics of the three shocks presented here are listed in Table 1. Event 1, from 2021-11-03, was exceptionally strong for an interplanetary shock. The shock was quasi-parallel (θ_{Bn} = 5–22°), with an observed compression ratio of $r = 4.4$ and fast mode Mach number M_{fm} = 5.9–6.2. These are comparable to the Earth's bow shock, and hence, ideal for us to test our approach to finding candidate downstream jets. The upstream plasma beta was $\beta_1 \sim 0.4$. The other two events were chosen to explore the low beta and low Mach number parameter ranges that are rare for the Earth's bow shock (Vuorinen et al. 2023). Event 2, from 1999-12-12, was oblique (θ_{Bn} = 46–54°), with an observed compression ratio of $r = 2.5$ and fast mode Mach number M_{fm} = 1.8–1.9. The upstream plasma beta was exceptionally low at $\beta_1 \sim 0.07$ ($\beta_1 \sim 0.03$ according to SWE). Event 3, from 2000-02-11, was rather quasi-parallel with θ_{Bn} = 35–39°, an observed compression ratio of $r = 2.4$, fast mode Mach number M_{fm} = 1.6–1.7, and upstream beta $\beta_1 \sim 0.3$.

4.1 Event 1

Wind recorded the strong, quasi-parallel interplanetary shock at 19:35 UT on 2021, November 3, at the L1 point. The left-hand side of Fig. 1 displays the main quantities, ±10 min, on each side of the shock. This event was first reported by Trotta et al. (2023), focusing on the shocklets seen up to ∼25 min upstream of the shock. The shocklets had durations of the order of ∼1–2 min, i.e. long compared to the variations of interest here. The shock had a compression ratio and Mach numbers comparable to those of the Earth's bow shock. Note, though, that the upstream plasma beta was relatively low ($\beta_1 \sim 0.4$) compared to typical bow shock conditions, and the upstream ion temperature anisotropy was high ($T_{1||}/T_{1\perp} = 1.5$). This anisotropy $T_{1||} > T_{1\perp}$ persisted in the downstream region. The V_n^{sh} ratio (Fig. 1 f; equation 6) was very steady in the upstream region and the flow slowed down to ∼0.25 in the downstream region, as expected from MHD. The different curves corresponding to the different $(\boldsymbol{n}, V_{sh}^{sc})$ estimates show the same behaviour with very little spread. The dynamic pressure ratio (Fig. 1 g; equation 7) had upstream variations on the time-scale of ∼1–2 min, probably due to the shocklets. It decreased to around 0.25 in the downstream region, as expected, for several minutes. The different curves display increasing spread after ∼19:41 UT. We can see distinct dynamic pressure pulses above the (blue) threshold of $2/r$ between 19:39 and 19:40 UT.

Let us examine these downstream jet candidates in more detail (zoom-in shown on the right-hand side of Fig. 1). The algorithm identifies 3–5 jets, depending on the shock estimate. The first three jets exceed the dynamic pressure threshold for all 20 estimates, and the fourth for 11 estimates, i.e. they are not sensitive to the shock parameter estimation. However, their pressure does not exceed the upstream dynamic pressure, as is the case for some magnetosheath jets. The duration of the pulses is 3–9 s (1–3 data points), as expected. This corresponds to a size of ∼2400–7100 km along the solar wind flow direction, or ∼34–72 d_i ($d_i \sim 98$ km in the downstream region). The dynamic pressure enhancements are accompanied by V_n^{sh} pulses, and also visible as slower instances in the $V_{X,GSE}$ in the spacecraft frame. More quantitatively in the shock frame, the jets have velocities of $\left\langle V_n^{sh} \sim -117\right\rangle$ to −126 km s^{-1}, which are ∼30 km s^{-1} (about 30–40 per cent) faster than the mean downstream $\left\langle V_{2n}^{sh}\right\rangle$ of −92 km s^{-1}. Therefore, the jet candidates are clearly super-Alfvénic but not quite supermagnetosonic with respect to the shock (downstream $V_A \sim$ 65 km s^{-1} and $V_{MS} \sim$ 145 km s^{-1}). The jet candidates are located in a longer duration density enhancement, and not solely individual density spikes. They feature a decrease in the ion temperature. Considering their magnetic field characteristics, they do not feature large changes in the magnetic field magnitude, and they are not centred on large field rotations (current sheets). Outflow exhausts of

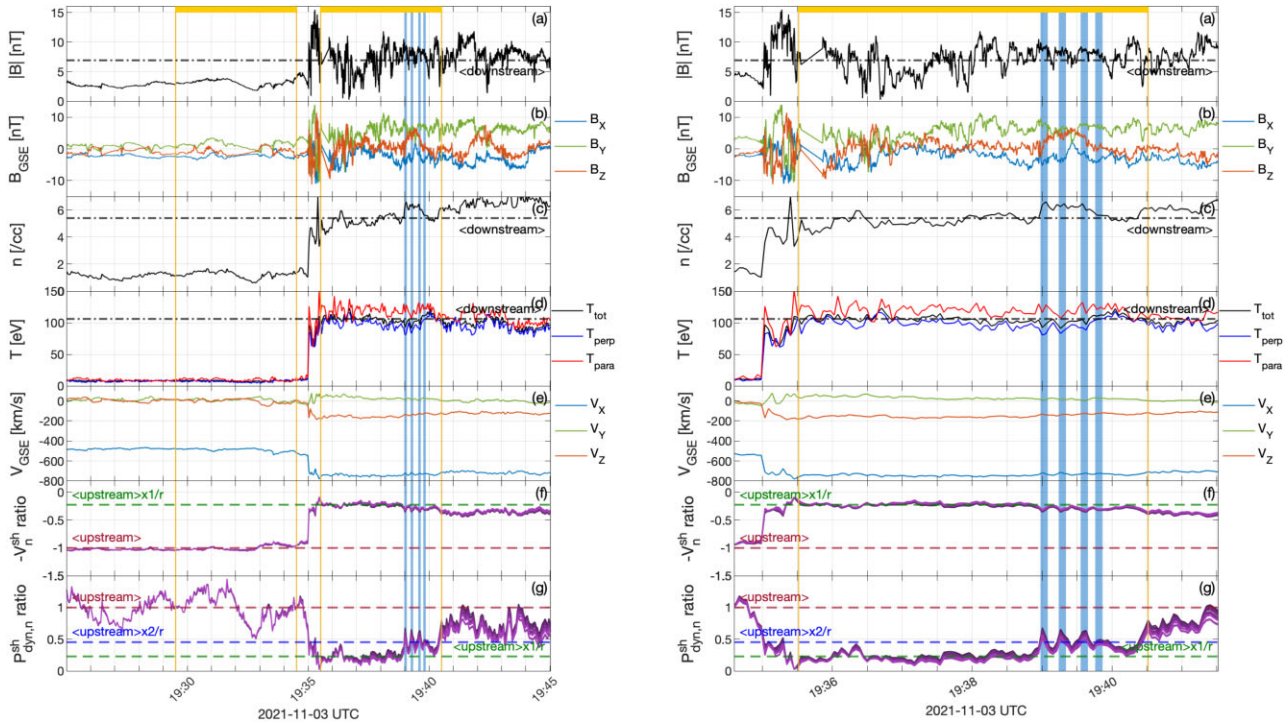

Figure 1. Event 1. From top to bottom: (a) magnetic field magnitude, (b) magnetic field components in GSE-coordinates, (c) ion density, (d) ion temperature, (e) ion velocity in GSE-coordinates, (f) $-V_{\rm n}^{\rm sh}$ ratio, and (g) $P_{\rm dyn,n}^{\rm sh}$ ratio (20 purple curves corresponding to different shock parameter estimates). Yellow bars and vertical lines mark the 5 min upstream and downstream windows, where temporal averages are calculated, indicated with dashed and dash–dotted horizontal lines, respectively. The jet candidates where the dynamic pressure ratio threshold is exceeded for at least 11 of the 20 estimates, shock estimates, are highlighted in blue. The right-hand side shows a zoom-in of the downstream region.

reconnecting current sheets would also be expected to feature some ion heating (e.g. Mistry et al. 2017), which is not the case here.

4.2 Event 2

Fig. 2 shows the very low beta interplanetary shock from 1999, December 12. At the time, Wind was located past the terminator and over 55 $R_{\rm E}$ to the dawn side of the Earth. Due to its location and the orientation of the IMF, Wind's magnetic connection to the bow shock (and foreshock) is possible. Indeed, around 15:10 UT, when $B_{\rm Z,\,GSE}$ decreased to ∼0 nT, the ion temperature increased to 3–40 eV for about 5 min, and the waves were more irregular (not shown). We interpret this as a brief distant foreshock crossing. However, during the ∼30 min before the IP shock arrival, the IMF orientation stayed steady, and there are no distinct signatures of the Earth's foreshock's influence at Wind's location. In particular, we note that ACE, which recorded this interplanetary shock at the L1 point at 15:15 UT, saw very similar wave activity upstream of the shock as Wind (not shown). We therefore attribute these upstream waves, visible both in the magnetic field and plasma data (Fig. 2), to the interplanetary shock and the solar wind. The upstream waves lead to large-amplitude upstream variations in dynamic pressure $P_{\rm dyn,n}^{\rm sh}$ with pulse durations of 3–15 s.

In the downstream region, similar dynamic pressure pulses are present. Note that, as the compression ratio $r = 2.5$, the diagnostic thresholds $[1/r, 2/r, 1] = [0.4, 0.8, 1]$. In other words, their separation is not as large as for $r = 4$. There are 2–7 jet candidates, of which the four highlighted in blue cross the $2/r$ threshold with over half the shock estimates and two with all estimates. Their durations are 3–6 s (1–2 data points) corresponding to a size of ∼1500–3000 km along the solar wind flow direction, or ∼10–20 $d_{\rm i}$ ($d_{\rm i} \sim 155$ km in the downstream region). The jets have a more negative $V_{\rm n}^{\rm sh}$ ratio than their surroundings. In the shock frame, they have velocities of $\langle V_{\rm n}^{\rm sh} \sim -117\rangle$ to -133 km s^{-1}, which are 26–43 km s^{-1} (29–47 per cent) faster than the mean downstream $\langle V_{\rm 2n}^{\rm sh}\rangle$ of -91 km s^{-1}. These jet candidates are sub-Alfvénic but supersonic with respect to the shock (downstream $V_{\rm A} \sim 148$ km s^{-1} and $V_{\rm S} \sim 73$ km s^{-1}). They are not simply density pulses, and most of them are colder than their surroundings. They are in phase with the magnetic field variations. The downstream dynamic pressure pulses are similar to the upstream variations, which implies these pass through the shock as it processes the plasma.

4.3 Event 3

Fig. 3 shows another low beta, quasi-parallel interplanetary shock from 2000, February 11. During this event, Wind was located near the L1 point. This shock was slightly weaker, with observed magnetic compression ratio <2. A notable feature of Event 3 are larger scale (over a minute) variations in $B_{\rm Y,\,GSE}$ and $V_{\rm Y,GSE}^{\rm sc}$. These same variations are present in $V_{\rm n}^{\rm sh}$ and $P_{\rm dyn,n}^{\rm sh}$, leading even to flow back towards the shock (positive $V_{\rm n}^{\rm sh}$ around 02:38:15 UT on the downstream side). Note also that the different (purple) curves begin to spread in the downstream region faster than in the other events. We attribute these larger-scale plasma motions to solar wind turbulence.

On the downstream side, there are 3–4 jet candidates, and three exceed the dynamic pressure threshold for all shock estimates. As the compression ratio $r = 2.4$, the diagnostic thresholds are again $[1/r, 2/r, 1] = [0.4, 0.8, 1]$. Two candidates are co-located with a $B_{\rm Y,\,GSE}$ sign change (i.e. a current sheet), while the first jet-

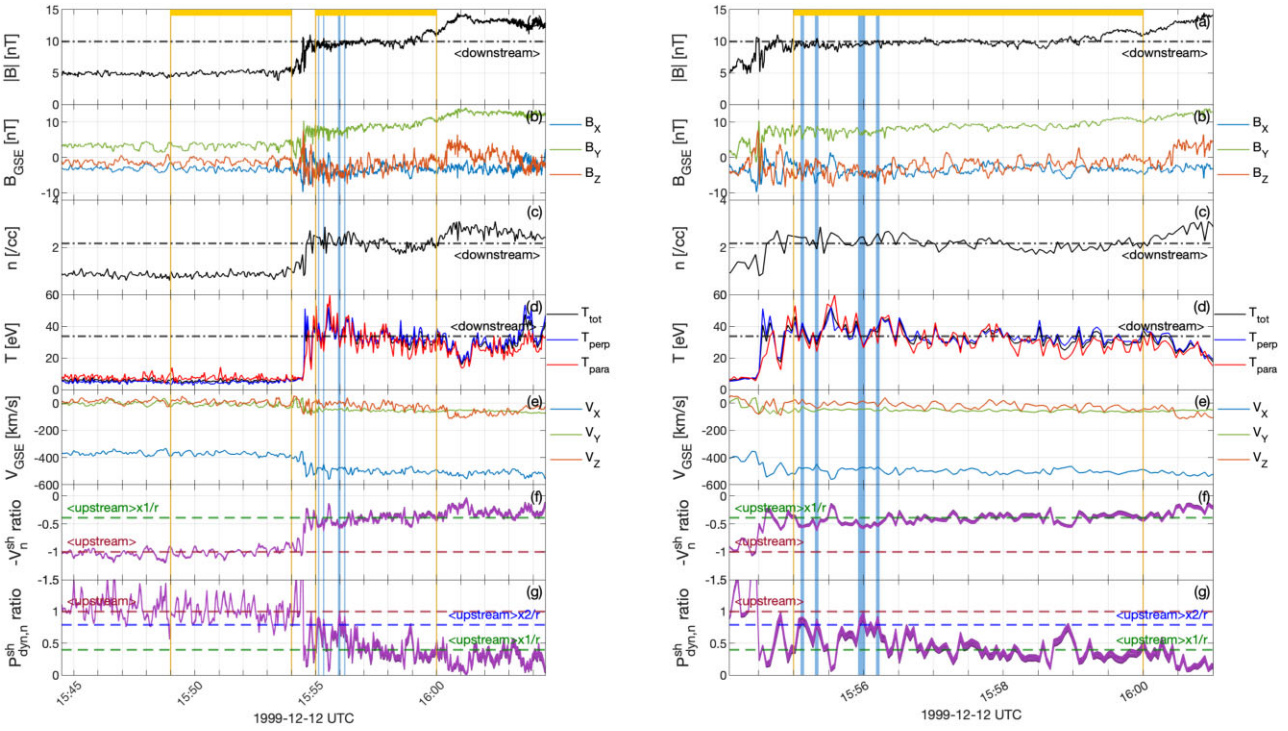

Figure 2. Event 2. Same format as Fig. 1.

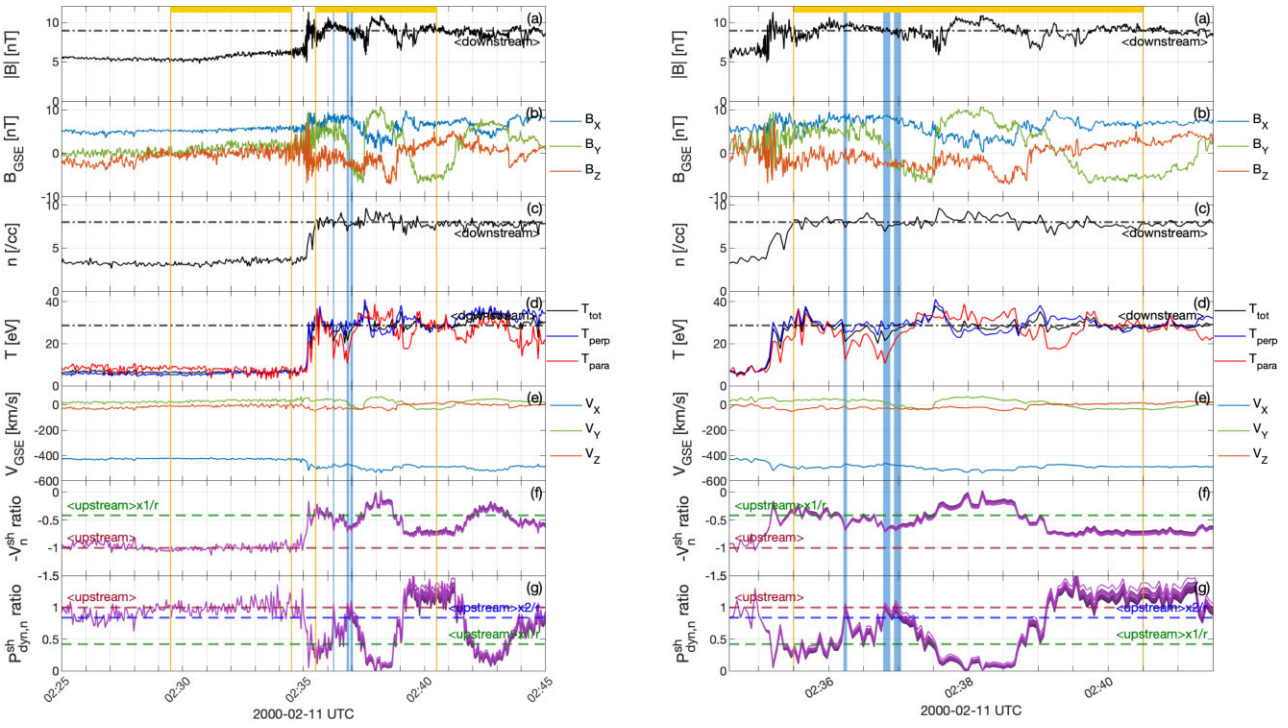

Figure 3. Event 3. Same format as Fig. 1.

like structure has relatively steady magnetic field. Their durations correspond to a size of ∼1500–3000 km along the solar wind flow direction, or ∼19–38 d_i (d_i ∼ 80 km in the downstream region). None of the jets is dominated by density enhancement, and they are all colder than the average downstream. They have a more negative V_n^{sh} ratio. In the shock frame, they have velocities of $\langle V_n^{sh} \rangle \sim -74$ to $-79\,km\,s^{-1}$, which are 20–45 $km\,s^{-1}$ (37–45 per cent) faster than the mean downstream $\langle V_{2n}^{sh} \rangle$ of $-54\,km\,s^{-1}$. (Note that this mean is affected by the large-scale variation.) These jet candidates are mildly super-Alfvénic but not supermagnetosonic with respect to the shock (downstream $V_A \sim 69\,km\,s^{-1}$ and $V_{MS} \sim 97\,km\,s^{-1}$). Some dynamic pressure fluctuations of similar duration are also present in

the upstream (foreshock) of Event 3, though not as distinct and large amplitude as in Event 2.

5 DISCUSSION AND CONCLUSIONS

We have introduced a method for identifying localized dynamic pressure enhancements (jets) downstream of interplanetary shocks. We have applied this approach to three shocks and found several jet candidates, which had similar properties as magnetosheath jets: they featured an enhanced flow away from the shock (by about 30–40 per cent in the shock frame), they were colder than the average downstream plasma, and they were not dominated by density enhancements nor B variations. The first shock had a similar Mach number and compression ratio as the Earth's bow shock, demonstrating the applicability of our analysis. The other two had lower plasma beta and Mach number, which widens the explored parameter range and can shed light on jet dynamics and formation mechanisms.

For a quantitative comparison with magnetosheath jets, we can consider the data set used in (Vuorinen et al. 2023), and select a subset that had upstream conditions similar to the three IP shocks ($M_A \lesssim 7$, $\theta_{Bn} \lesssim 50^\circ$; 657 jets). These magnetosheath jets have a median dynamic pressure ratio of 0.89 (mode 0.62), in comparison to 0.46–0.60 for the four IP jets in Event 1. Likewise, the magnetosheath jets have a median $V_{X,GSE}/V_{SW} = 0.38$ (mode 0.36), which matches Event 1 jets' V_n^{sh} ratio ∼0.33. The median flow-parallel size of these magnetosheath jets is 0.58 $R_E \sim 40\,d_i$ (mode 0.31 $R_E \sim 20\,d_i$), which is similar to the ∼40–50 d_i scale observed for Event 1. (Note that we are limited to $> 34\,d_i$ by the instrument cadence in this event.) The IP jets in the low Mach number, low beta Events 2 and 3 were relatively stronger, as the compression ratio r was lower. Their dynamic pressure ratios were 0.85–0.92 and 0.99–1.01, and V_n^{sh} ratios 0.53–0.61 and 0.66–0.71, respectively. On the other hand, their sizes were smaller, 10–20 d_i and 19–38 d_i, respectively. Note that we observe jets up to ∼2, 200, ∼300, and ∼ 700 d_i downstream of the IP shocks in Events 1–3, respectively. The typical subsolar magnetosheath thickness is only ∼3 $R_E \sim 200\,d_i$, whereupon the jets would impact the magnetopause.

All three interplanetary shocks studied here were quasi-parallel or oblique ($\langle\theta_{Bn}\rangle$ = 12–49°), featured a complex magnetic transition, and were associated with foreshock wave activity – favourable conditions for magnetosheath jet formation. While some interplanetary shocks at 1 au have particle and wave foreshocks (Kajdič et al. 2012), it is important to note that the level of activity and the compressibility of the waves are generally lower than at planetary bow shocks (Blanco-Cano et al. 2016). Interplanetary counterparts of Short Large Amplitude Structures (SLAMS; e.g. Schwartz & Burgess (1991); Lucek et al. (2008)), which have d$B/B > 2$ and are common in planetary foreshocks, have not been reported to date. Shocklets (d$B/B \lesssim 2$) have been reported upstream of interplanetary shocks on three occasions (Lucek & Balogh 1997; Wilson et al. 2009; Trotta et al. 2023), including in Event 1 analysed here, but at much larger temporal/spatial scales than expected for jets. In the extremely low beta Event 2, the direct transmission of upstream dynamic pressure variations related to foreshock waves would seem to be a plausible explanation for the downstream jet-like structures. However, we do not expect this process to be the same as in the (ion) Vlasov-hybrid simulations of Palmroth et al. (2018) and Suni et al. (2021) because the magnetic fluctuations observed here are not as compressive as the d$B/B > 2$ structures they studied. On the other hand, interplanetary shocks have been observed to feature ripples at scales similar to the jet candidates ($\lesssim$100 d_i; Kajdič et al. (2019)), as well as soliton-like whistler precursors (Wilson et al. 2017). The latter could indicate whistler-driven shock reformation under low Mach number ($M_A \lesssim 3$), low beta ($\beta \lesssim 1$) conditions. The proposed jet formation mechanisms related to shock reformation and/or shock non-stationarity (e.g. Hietala et al. 2009; Raptis et al. 2022) could thus potentially operate under interplanetary shock conditions. In the case of Event 3, two jet candidates are located at a larger-scale current sheet, which may be indicative of driving by an upstream magnetic field directional discontinuity as in e.g. (Archer et al. 2012). Therefore, the interplanetary shock jets presented here possibly show examples of both shock reformation/non-stationarity and discontinuity driving, while the transmission of compressive magnetic structures would be replaced with transverse waves. None the less, much larger statistics of interplanetary shock jets are needed to draw conclusions on their formation. Future work should, thus, include further investigations at 1 au with Wind and MagnetophericMultiScale (MMS; Burch et al. (2016)), as well as interplanetary shocks observed at various heliocentric distances by ParkerSolarProbe (Fox et al. 2016) and SolarOrbiter (Müller et al. 2013).

ACKNOWLEDGEMENTS

The work of HH is supported by the Royal Society award URF\R1\180671. HH thanks discussions at the International Space Science Institute (ISSI) in Bern, through ISSI International Team project #465 (Foreshocks Across The Heliosphere: System Specific or Universal Physical Processes?). The work of DT is supported from the European Union's Horizon 2020 research and innovation programme under grant agreement No. 101004159 (SERPENTINE, www.serpentine-h2020.eu). Some of the work was supported by the Geospace Environment Modeling Focus Group 'Particle Heating and Thermalization in Collisionless Shocks in the Magnetospheric multi-scale mission (MMS) Era' led by L. B. Wilson III. LV acknowledges the financial support of the University of Turku Graduate School.

DATA AVAILABILITY

The data used in this study are available at the Coordinated Data Analysis Web (CDAWeb) at https://cdaweb.gsfc.nasa.gov/. Data analysis was performed using the IRFU-Matlab analysis package available at https://github.com/irfu/irfu-matlab/ and SerPyShock tools available at https://github.com/trottadom/SerPyShock.

REFERENCES

Archer M. O., Horbury T. S., Eastwood J. P., 2012, J. Geophys. Res.: Space Physics, 117, A05228,
Blanco-Cano X., Kajdič P., Aguilar-Rodríguez E., Russell C. T., Jian L. K., Luhmann J. G., 2016, J. Geophys. Res.: Space Phys., 121, 992
Burch J., Moore T., Torbert R., Giles B.-h., 2016, Space Sci. Rev., 199, 5
Coburn J. T., Chen C. H. K., Squire J., 2022, J. Plasma Phys., 88, 175880502
Eriksson E. et al., 2016, J. Geophys. Res.: Space Physics, 121, 9608
Fox N. J. et al., 2016, Space Sci. Rev., 204, 7
Gunell H., Hamrin M., Nesbit-Östman S., Krämer E., Nilsson H., 2023, Sci. Adv., 9, eadg5703
Guo J. et al., 2022, J. Geophys. Res.: Space Physics, 127, e30477
Hao Y., Lembege B., Lu Q., Guo F., 2016, J. Geophys. Res.: Space Phys., 121, 2080
Hietala H. et al., 2009, Phys. Rev. Lett., 103, 20
Hietala H. et al., 2012, Ann. Geophys., 30, 33
Kajdič P., Preisser L., Blanco-Cano X., Burgess D., Trotta D., 2019, ApJ, 874, L13

Kajdič P., Blanco-Cano X., Aguilar-Rodriguez E., Russell C. T., Jian L. K., Luhmann J. G., 2012, J. Geophys. Res.: Space Phys., 117, A06103
Karimabadi H. et al., 2014, Phys. Plasmas, 21 062308
Karlsson T. et al., 2018, Ann. Geophys., 36, 655
Kilpua E. K. J., Lumme E., Andreeova K., Isavnin A., Koskinen H. E. J., 2015, J. Geophys. Res.: Space Phys., 120, 4112
Koller F., Plaschke F., Temmer M., Preisser L., Roberts O. W., Vörös Z., 2023, J. Geophys. Res.: Space Phys., 128, e2023JA031339
LaMoury A. T., Hietala H., Plaschke F., Vuorinen L., Eastwood J. P., 2021, J. Geophys. Res.: Space Phys., 126, e29592
Lepping R. P. et al., 1995, Space Sci. Rev., 71, 207
Lin R. P. et al., 1995, Space Sci. Rev., 71, 125
Liu T. Z., Hietala H., Angelopoulos V., Omelchenko Y., Roytershteyn V., Vainio R., 2019, Geophys. Res. Lett., 46, 7929
Liu T. Z., Hietala H., Angelopoulos V., Vainio R., Omelchenko Y., 2020b, J. Geophys. Res.: Space Phys., 125, e27709
Liu T. Z., Hietala H., Angelopoulos V., Angelopoulos V., Omelchenko Yuri , Omelchenko Y., Vainio R., Plaschke F., 2020a, J. Geophys. Res., 125, e27710
Lucek E. A., Balogh A., 1997, Geophys. Res. Lett., 24, 2387
Lucek E. A., Horbury T. S., Dandouras I., Re H., 2008, J. Geophys. Res., 113, 1
Mistry R., Eastwood J. P., Phan T. D., Hietala H., 2017, J. Geophys. Res.: Space Phys., 122, 5895
Müller D., Marsden R. G., St. Cyr O. C., Gilbert H. R., Solar Orbiter Team, 2013, Sol. Phys., 285, 25
Ogilvie K. W. et al., 1995, Space Sci. Rev., 71, 55
Palmroth M. et al., 2018, Ann. Geophys., 36, 1171
Schwartz S. J., 2000, in Paschmann G., Daly P. W., eds., Analysis Methods for Multi-Spacecraft Data. ISSI/ESA, Netherlands, p. 249
Plaschke F., Hietala H., Angelopoulos V., 2013, Ann. Geophys., 31, 1877
Plaschke F. et al., 2018, Space Sci. Rev., 214, 81
Plaschke F., Jernej M., Hietala H., Vuorinen L., 2020, Ann. Geophys., 38, 287
Preisser L., Blanco-Cano X., Kajdič P., Burgess D., Trotta D., 2020, ApJ, 900, L6
Raptis S., Karlsson T., Plaschke F., Kullen A., Lindqvist P.-A., 2020, J. Geophys. Res.: Space Physics, 125, e2019JA027754
Raptis S., Karlsson T., Vaivads A., Pollock C., Plaschke F., Johlander A., Trollvik H., Lindqvist P.-A., 2022, Nat. Commun., 13, 598
Schwartz S. J., Burgess D., 1991, Geophys. Res. Lett., 18, 373
Suni J. et al., 2021, Geophys. Res. Lett., 48, e95655
Tinoco-Arenas A., Kajdič P., Preisser L., Blanco-Cano X., Trotta D., Burgess D., 2022, Front. Astron. Space Sci., 9, 793195
Trotta D. et al., 2022, Frontiers in Astronomy and Space Sciences, 9 1005672
Trotta D., Hietala H., Horbury T., Dresing N., Vainio R., Wilson L., III, Plotnikov I., Kilpua E., 2023, MNRAS, 520, 437
Vuorinen L., Hietala H., Plaschke F., 2019, Ann. Geophys., 37, 689
Vuorinen L., Hietala H., Plaschke F., LaMoury A. T., 2021, J. Geophys. Res.: Space Physics, 126, e29188
Vuorinen L., Hietala H., LaMoury A. T., Plaschke F., 2023, J. Geophys. Res.: Space Physics, 128, e2023JA031494
Wilson L. B., III, Koval A., Szabo A., Stevens M. L., Kasper J. C., Cattell C. A., Krasnoselskikh V. V., 2017, J. Geophys. Res.: Space Physics, 122, 9115
Wilson L. B., III et al., 2021, Rev. Geophys., 59, e2020RG000714
Wilson L. B., III, Cattell C. A., Kellogg P. J., Goetz K., Kersten K., Kasper J. C., Szabo A., Meziane K., 2009, J. Geophys. Res.: Space Physics, 114, A10106

This paper has been typeset from a TEX/LATEX file prepared by the author.